

## Article

# Efficient Removal of Representative Chemical Agents by Rapid and Sufficient Adsorption via Magnetic Graphene Oxide Composites

Jina Wu <sup>1</sup>, Gang Qu <sup>1</sup>, Long Yan <sup>1</sup>, Ruixue Wang <sup>2</sup>, Peiwen Guo <sup>2</sup>, Yang Yang <sup>1,\*</sup> and Xiaosen Li <sup>1,\*</sup>

<sup>1</sup> State Key Laboratory of NBC Protection for Civilian, Beijing 102205, China; wujina09@163.com (J.W.); qu0612@126.com (G.Q.); yanl\_allen@163.com (L.Y.)

<sup>2</sup> College of Mechanical and Electrical Engineering, Beijing University of Chemical Technology, Beijing 100029, China; wrx@mail.buct.edu.cn (R.W.); 2021200630@buct.edu.cn (P.G.)

\* Correspondence: ricd\_yihui@163.com (Y.Y.); momentday@126.com (X.L.); Tel.: +86-10-69760259 (Y.Y. & X.L.)

**Abstract:** Chemical agents pose a significant threat to social security, highlighting the crucial role of representative chemical agents adsorption in ensuring the safety our environment. This study explored the application of Magnetic Graphene Oxide Nanoplatelet Composites (MGONCs) in adsorbing the representative chemical agents such as Lewisite (L), O-ethyl S-2-diisopropylaminoethyl methylphosphonothiolate (VX), Sarin (GB), and Soman (GD). MGONCs were synthesized through a physical blending method, with the combination of graphene oxide (GO) and Fe<sub>3</sub>O<sub>4</sub> nanoparticles at a mass ratio of 1:1. Optimization of the adsorption process involved investigating the effects of contact time, temperature, and adsorbent dosage. Remarkably, the adsorption rate of L and VX exceeded 99% when the dosage of MGONCs was 2.5 mg, with a contact time of 30 s at room temperature. Furthermore, GB and GD achieved maximum adsorption rates after a contact time of 20 min, with the dosages of MGONCs at 10 mg and 20 mg, respectively. Characterization of the magnetic composite was accomplished through XRD, TEM, VSM, FTIR, TGA, and BET analyses. Kinetic analysis revealed that the adsorption mechanism of GB and GD on MGONCs followed pseudo-second-order (PSO) kinetics, exhibiting a high regression coefficient. The calculated  $q_e$  values were 0.103125 mg/g and 0.081349 mg/g, respectively. This research demonstrated the feasibility of utilizing MGONCs as highly efficient adsorbents for representative chemical agents, particularly in on-site sampling scenarios.

**Keywords:** graphene oxide; Fe<sub>3</sub>O<sub>4</sub>; absorption; chemical agents



**Citation:** Wu, J.; Qu, G.; Yan, L.; Wang, R.; Guo, P.; Yang, Y.; Li, X. Efficient Removal of Representative Chemical Agents by Rapid and Sufficient Adsorption via Magnetic Graphene Oxide Composites. *Appl. Sci.* **2023**, *13*, 10731. <https://doi.org/10.3390/app131910731>

Academic Editor: Vasili Perebeinos

Received: 3 September 2023

Revised: 22 September 2023

Accepted: 25 September 2023

Published: 27 September 2023



**Copyright:** © 2023 by the authors. Licensee MDPI, Basel, Switzerland. This article is an open access article distributed under the terms and conditions of the Creative Commons Attribution (CC BY) license (<https://creativecommons.org/licenses/by/4.0/>).

## 1. Introduction

Chemical agents pose a significant threat to human safety [1,2]. They could be categorized as incapacitating agents, which diminish people's fighting abilities without long-term effects, and lethal agents, which can even kill humans [3]. Figure 1 illustrates the structures of Lewisite (L), O-ethyl S-2-diisopropylaminoethyl methylphosphonothiolate (VX), Sarin (GB), and Soman (GD), which are confirmed lethal agents. These agents typically attack the respiratory system or the skin [4]. VX, GB, and GD inhibit the activity of the cholinesterase enzyme, leading to severe damage to the central nervous system [5]. Moreover, these agents are highly soluble in water or organic solvents, causing harm even at extremely low concentrations [6]. Despite the Chemical Weapons Convention (CWC) which came into effect in 1997, chemical agents continue to threaten civilian and military populations due to their destructive capacity [7]. The concealment of chemical agents usage and the difficulty of detecting residual agents in the environment underscore the importance of developing reliable traceable detection methods. Such methods are crucial for providing evidence of chemical weapons and improving medical treatment for poisoned individuals [8].

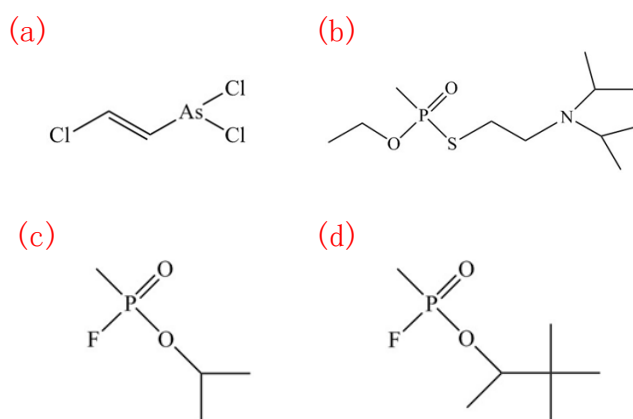


**Figure 1.** Structural formula of several typical chemical agents: (a) L; (b) VX; (c) GB; (d) GD.

To enhance the extraction and enrichment of chemical agents for retrospective detection, the adsorbent used in sample preparation should be well-designed, easy to use, insensitive, and posing no additional safety concerns. Previous studies had employed various materials such as activated carbon [9–11], metal oxide nanoparticles [12–17], and metal–organic framework structures (MOFs) [18–21] for chemical agents and simulant adsorption. For example, Hyejin Yu et al. [22] used chitosan-derived porous activated carbon to remove the simulant agents for chemical weapons, achieving a saturation adsorption capacity of approximately  $412 \text{ mg}\cdot\text{g}^{-1}$  carbon after 2 days. Marc Florent et al. [23] utilized a co-precipitation method to prepare zinc–iron and copper–iron mixed (hydr) oxides, finding that the zinc–iron samples exhibited higher activity than the copper–iron samples when exposed to surrogates for 5 days. However, the adsorption capacity of these materials, especially within a relatively short timeframe, still need to be improved.

Graphene oxide (GO) has garnered significant attention in recent decades due to its unique properties. GO is highly oxidized graphite with abundant oxygen-containing functional groups ( $-\text{OH}$ ,  $-\text{COOH}$ ,  $-\text{CHO}$ , and  $-\text{COC}-$ ) on its surface [24–26]. It shares a similar high surface area to graphene, and the high surface-to-volume ratio of GO offers benefits in adsorption, including rapid equilibrium rates [27–30]. Jiri Henych et al. [31] prepared  $\text{TiO}_2$  nanoparticles supported on GO flakes and studied their adsorption properties for the simulant agents, highlighting the importance of GO in increasing surface area and improving adsorption capacity. Martin Stastn et al. [32] demonstrated a simple low-temperature water-based method to create a novel nanocomposite,  $\text{GO@MnO}_2$ , and evaluated its adsorption activity with nerve agent simulants, achieving an almost complete degradation of dimethyl methyl phosphonate (DMMP) and triethyl phosphate (TEP) within 2 h. Additionally, GO showed great potential as an adsorbent for sample preparation. However, these materials were a challenge to prepare and separate from solutions during experiments [33]. An effective approach was to employ magnetic solid-phase extraction (MSPE). Magnetite ( $\text{Fe}_3\text{O}_4$ ) was widely used in MSPE due to its high magnetic moments, small size, biocompatibility, and ease of preparation [34]. With the assistance of  $\text{Fe}_3\text{O}_4$ , the separation of the sorbent (GO) from the sample was easily achieved by applying an external magnetic field, significantly reducing separation time compared to centrifuging or filtering methods [33,35].

Although the GO materials show great adsorption abilities, insufficient research focus on the adsorption of these chemical agents. In part, most studies applied the GO materials to the hydrolysis products or the simulant to study the adsorption due to the difficulty of acquiring these chemical agents. However, it is still particularly important to investigate the adsorption of actual and representative chemical agents. Furthermore, in consideration of the highly toxic and lethal properties, the major point for the adsorbing material should be the adsorption rate. In this study, Magnetic Graphene Oxide Nanoplatelet Composites (MGONCs) were synthesized by physically blending GO and  $\text{Fe}_3\text{O}_4$  and were successfully employed as adsorbents for L, VX, GB, and GD. The adsorption rate was optimized by ad-

justing contact time, temperature, and adsorbent dosage. Notably, the results demonstrated that chemical agents could be effectively adsorbed within 20 min. Furthermore, the adsorption kinetics and mechanisms were investigated in detail. The results indicated that the materials prepared in the research obtained good adsorption properties and showed great potential for the removal of chemical agents. The excellent adsorption properties provided the potential to apply the materials in special aqueous purification devices for adsorbing chemical agents. Moreover, we also provide recommendations on the application prospects in the field of protection suits or gas masks. In addition, due to the magnetic characteristics, the adsorbed material could be easily separated compared to other adsorption materials, which offers the potential for absorbing chemical agents in exposed environments.

## 2. Materials and Methods

### 2.1. Materials

Magnetic frame (Magnetic 3700 Gauss, Dynamag-2, ThermoFisher Company, Waltham, MA, USA); 5350 Oscillating heater (Eppendorf Company, Hamburg, Germany). Graphene oxide (SIGMA Company, St. Louis, MO, USA, product number: 763713); acetone, purity greater than 99.5% (J&K Company, Beijing, China); methanol, purity greater than 99% (J&K Company, Beijing, China); dichloromethane, purity greater than 99% (J&K Company, Beijing, China); acetonitrile, purity greater than 99% (J&K Company, Beijing, China); concentrated hydrochloric acid; concentrated ammonia, analytical purity (domestic, Beijing, China); butyl mercaptan (BT), purity greater than 99% (J&K Company, Beijing, China); L, VX, GB, GD, purity greater than 90% (micro-synthesized in-house of the Laboratory of Analytical Chemistry of Research Institute of Chemical Defence, Beijing, China).

### 2.2. Preparation of Magnetic Graphene Oxide Nanoplatelet Composites (MGONCs)

#### 2.2.1. Synthesis of Magnetic Nanoparticles (MNs)

The magnetic nanoparticles (MNs) were fabricated using the hydrothermal synthesis method [36]. Initially, 0.786 g (2.00 mM) of ferric ammonium sulfate hexahydrate and 1.933 g (4.00 mM) of ferric ammonium sulfate dodecahydrate were quickly mixed under the protection of N<sub>2</sub>. This mixture was then added to a 15 mL (8 mol/L) aqueous ammonia solution. Subsequently, the solution was heated and incubated at 80 °C for 30 min. Afterward, the synthesized iron oxide was washed at least 20 times with deionized water, resulting in the precipitation of the iron oxide powders at the bottom of the container with the aid of a magnet. These precipitated powders were separated and dried at 50 °C for 10 h, yielding vacuum-dried magnetic nanoparticles. To enhance homogeneity and increase the specific surface area, the magnetic nanoparticles were ground for 20 min using a grinder at a speed of 100 r/min. Finally, the magnetic nanoparticles were collected, weighed, and used as samples.

#### 2.2.2. Synthesis of MGONCs

GO (SIGMA Company, St. Louis, MO, USA) and MNs were mixed at different mass ratios (1:0.11, 1:0.25, 1:0.43, 1:0.6, 1:1, 1:1.5, 1:2.33, 1:4, 1:9 for GO: MNs, respectively) and subjected to full oscillation for 20 min to obtain Fe<sub>3</sub>O<sub>4</sub>@GO, which could be recognized as the Magnetic Graphene Oxide Nanoplatelet Composites (MGONCs). Each of the prepared materials was weighed at 10 mg, and 200 µL of dichloromethane solution was added. Then, the mixture was placed on a magnetic stand for magnetic separation in a sequential manner.

The resulting solutions are depicted in Figure 2a. It was observed that when the mass ratios of GO:MNs were 1:0.43 and 1:0.6, the magnetic separation time for the obtained magnetic nanocomposite exceeded 30 s. On the other hand, when the mass ratios of GO:MNs were 1:0.11 and 1:0.25, effective magnetic separation could not be achieved within 10 min, failing to meet the requirements of subsequent magnetic solid-phase extraction methods. Only when the ratio was ≤1:1, the magnetic separation rate could reach 2–3 s, as shown in Figure 2b.

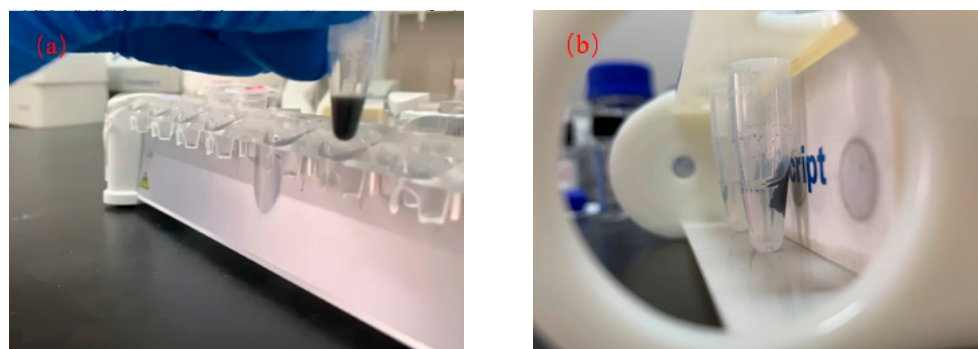


**Figure 2.** (a) Adsorption of magnetic composite materials; (b) magnetic phase separation of composite materials when GO:MNs  $\leq$  1:1.

Based on previous research, the mass ratio of GO:MNs was optimized at 1:1 for the synthesis of MGONCs. GO and MNs were weighed accurately to 500 mg each. The grinding process was performed using a mortar grinding instrument through the physical blending method. The grinding speed was set at 100 rad/min, and the total grinding time was 30 min. Subsequently, the magnetic nanocomposite materials obtained after grinding were weighed carefully.

### 2.3. Adsorption Experiment

To investigate the adsorption of representative chemical agents (L, VX, GB, and GD) by MGONCs, a solution of dichloromethane (200  $\mu$ L) mixed with each chemical agent (1  $\mu$ g) was injected into a centrifuge tube containing MGONCs (10 mg). The centrifuge tube was then placed in a 5350 oscillating heater (Eppendorf Company, Hamburg, Germany) at 1000 rpm oscillation. Different levels of adsorption time and temperature were fully optimized. The centrifuge tube was removed after the capturing process and placed in a magnetic frame (Magnetic 3700 Gauss, Dynamag-2, ThermoFisher Company, Waltham, MA, USA). The supernatant was carefully collected using a pipette. Finally, the amounts of L, VX, GB, and GD were estimated by analyzing the supernatant solution using gas chromatography-mass spectrometry (GC-MS).

### 2.4. Evaluation of Adsorption Performance

In order to investigate the mechanism and adsorption ability of MGONCs adsorbents on the chemical agents, a series of adsorption experiments were completed. The adsorption rate of MGONCs for L, VX, GB, and GD were determined using Equation (1):

$$\eta = \frac{(C_0 - C_t)}{C_0} \times 100\% \quad (1)$$

where  $C_0$  is the initial concentration of solution (mg/L);  $C_t$  is the analyte concentration at time  $t$  (min) (mg/L).

The adsorption capacity of MGONCs for L, VX, GB, and GD were determined using Equation (2):

$$q_t = \frac{(C_0 - C_t) \times V}{M} \quad (2)$$

where  $V$  is the volume of used solution (L) and  $M$  is the mass of adsorbent (g).

### 2.5. Instrumentation

Quantitative determination of the adsorption amounts for L, VX, GB, and GD was carried out using the Thermo Trace GC-Thermo DSQ II mass spectrometry system and Thermo Trace 1310 GC-Thermo ISQ 7000 mass spectrometry system (ThermoFisher Company, Waltham, MA, USA).

X-ray diffraction (XRD) patterns of the MGONCs powder were obtained using a Philips X'Pert X-ray diffractometer (Philips, Amsterdam, The Netherlands) equipped with  $\text{CuK}_{(\alpha)}$  radiation at 40 mA and 40 kV. The samples were scanned from  $2\theta$  of  $10^\circ$  to  $80^\circ$  with a step increment of  $0.02^\circ$ .

Transmission Electron Microscopy (TEM) studies were conducted using a JEOL 2100F instrument (JEOL, Tokyo, Japan) with an accelerating voltage of 200 kV. For TEM measurements, the MGONCs were dispersed in deionized water using ultrasonication and deposited onto carbon-coated TEM grids.

Fourier Transform Infrared (FTIR) spectra of the samples were recorded using a Nicolet 6700 FTIR spectrometer (ThermoFisher Company, Waltham, MA, USA) in the wavenumber range of  $4000$  to  $400\text{ cm}^{-1}$ .

Saturation magnetization ( $M_s$  or  $B_s$ ) was measured using a vibrating sample magnetometer (Quantum Design, San Diego, CA, USA) under a maximum applied field of  $\pm 10,000$  Oe.

Thermogravimetric analysis (TGA) was performed on a Q600-1126-SDT instrument provided by TA Instruments (TA, New Castle, DE, USA). The thermogravimetric and differential scanning calorimetric data were obtained. The run for MGONCs was conducted using a 4.176 mg sample with experimental settings at a heating rate of  $10.00\text{ }^\circ\text{C}/\text{min}$ , ranging from  $0\text{ }^\circ\text{C}$  to  $800\text{ }^\circ\text{C}$  in air ( $10\text{ mL}/\text{min}$ ).

Nitrogen ( $\text{N}_2$ ) adsorption–desorption isotherms were measured at  $-196\text{ }^\circ\text{C}$  with an ASAP 2020 (Micromeritics, Norcross, GA, USA). The samples were degassed to a continuous vacuum ( $10^{-4}$  Torr) at  $90\text{ }^\circ\text{C}$  before analysis. The adsorption isotherms were used to calculate the Braunauer, Emmet, Teller (BET) surface area.

### 3. Results and Discussion

#### 3.1. Characterization of MGONCs

##### 3.1.1. XRD

The polycrystalline structure of the MNs and MGONCs were determined using X-ray diffraction (XRD). Figure 3 displays the X-ray diffraction pattern of the MNs and MGONCs. The diffraction peaks of MNs were observed at  $2\theta$  values of  $30.1^\circ$ ,  $35.4^\circ$ ,  $43.0^\circ$ ,  $53.4^\circ$ ,  $57.9^\circ$ , and  $62.5^\circ$ , corresponding to electron diffraction peaks at positions (220), (311), (400), (422), (511), and (440), respectively. The results were consistent with  $\text{Fe}_3\text{O}_4$  nanoparticles and well-matched with JCPDS card No. 22-1086 [37]. For MGONCs, in addition to the diffraction peaks observed above, there was also a diffraction peak at  $2\theta$  values of  $10.8^\circ$ , which could be attributed to the diffraction peak of the graphene oxide crystal plane. Based on these findings, the successful syntheses of  $\text{Fe}_3\text{O}_4$  nanoparticles and MGONCs were confirmed.

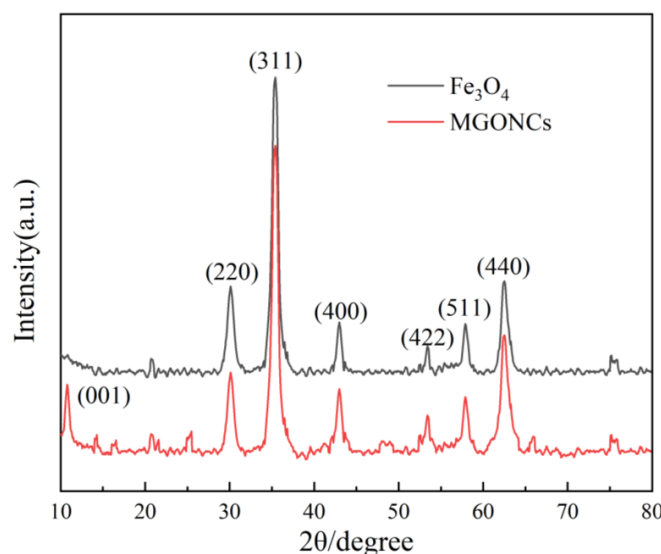


**Figure 3.** X-ray diffraction pattern of  $\text{Fe}_3\text{O}_4$  nanoparticles.

### 3.1.2. TEM

The TEM images of the  $\text{Fe}_3\text{O}_4$  nanoparticles are presented in Figure 4a. Approximately 200  $\text{Fe}_3\text{O}_4$  nanoparticles were randomly selected, and their particle diameters were measured, resulting in the histogram displayed in Figure 4b. The analysis revealed that 78% of the nanoparticles exhibited a particle size distribution ranging from 6 to 8 nm. The average size of the prepared  $\text{Fe}_3\text{O}_4$  nanoparticles was calculated to be  $7.32 \pm 1.12$  nm.

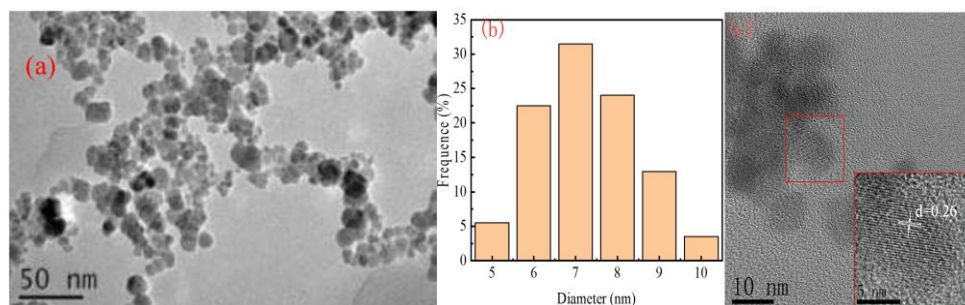


**Figure 4.**  $\text{Fe}_3\text{O}_4$  nanoparticles: (a) TEM image; (b) particle size distribution histogram; (c) high-resolution image of a single  $\text{Fe}_3\text{O}_4$  nanoparticle.

Figure 4c shows a captured TEM image of a single  $\text{Fe}_3\text{O}_4$  nanoparticle, clearly demonstrating the nearly round shape. Furthermore, a high-resolution image was obtained, which indicated a lattice spacing of approximately 0.26 Å, corresponding to the (220) lattice. This observation confirmed that the  $\text{Fe}_3\text{O}_4$  nanoparticles possessed good crystallization properties.

Figure 5a displays the TEM image of MGONCs, confirming the homogeneous distribution of  $\text{Fe}_3\text{O}_4$  nanoparticles supported on the surface of GO. The electron-selected area diffractions, depicted by the circular patterns in Figure 5b, further supported this observation. The positions of the electron diffraction peaks were categorized as (220), (311), (400), (422), (511), and (440), which was consistent with the results obtained from X-ray diffraction (XRD) [38]. These diffraction patterns indicated that the MGONCs obtained the face-centered cubic structure.

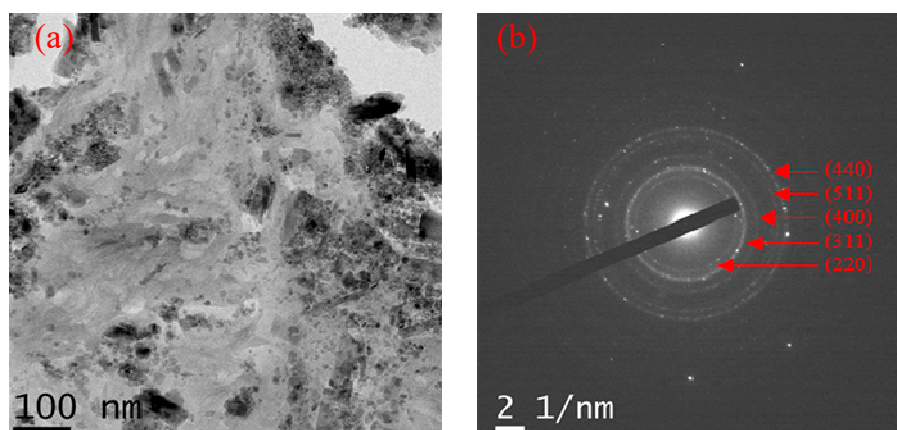


**Figure 5.** Characterization results of MGONCs: (a) TEM image; (b) selected area electron diffraction pattern.

### 3.1.3. FTIR

The results of the FTIR analysis for the surfaces of  $\text{Fe}_3\text{O}_4$ , GO, and MGONCs are presented in Figure 6. The broad band observed in the  $3400\text{--}3000\text{ cm}^{-1}$  region corresponds to the stretching vibration of  $-\text{OH}$  groups. The absorption peak at a wave number of  $1717.74\text{ cm}^{-1}$  was attributed to the  $\text{C}=\text{O}$  stretching vibration from carbonyl or carboxyl groups, while the peak at  $1610.00\text{ cm}^{-1}$  corresponded to the  $\text{C}=\text{C}$  aromatic stretching vibration. The peak at  $1221.38\text{ cm}^{-1}$  was associated with  $\text{C}-\text{O}$  bonds. Additionally, the strong  $\text{Fe}-\text{O}$  bond in  $\text{Fe}_3\text{O}_4$  was indicated by the low stretching vibrations observed at

598.37  $\text{cm}^{-1}$  [33,39]. The surface of the GO samples, C=O bonds, C–O peaks, and multiple peaks of O–H vibrations were observed. This indicated that the functional groups on the surface of MGONCs are predominantly derived from GO. In contrast, the  $\text{Fe}_3\text{O}_4$  nanoparticles mainly contributed to the magnetic properties. The combination of GO with magnetic nanoparticles resulted in a mixture that possessed both magnetic properties and a large number of active functional groups for subsequent experiments.

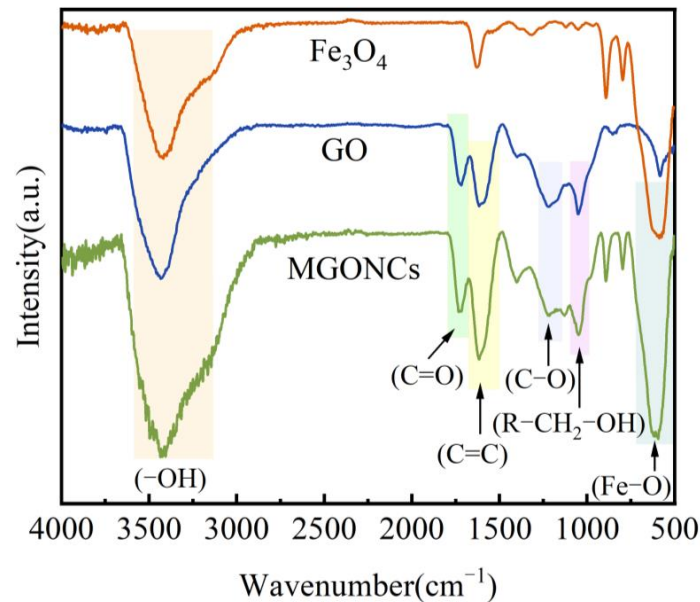


**Figure 6.** FTIR characterization chart of  $\text{Fe}_3\text{O}_4$ , GO, and MGONCs.

#### 3.1.4. VSM

The saturation magnetization ( $M_S$ ) was applied to evaluate the magnetic properties for  $\text{Fe}_3\text{O}_4$  nanoparticles. The result of VSM (shown in Figure 7) confirmed the ferromagnetic property for both  $\text{Fe}_3\text{O}_4$  and MGONCs. Typically, the  $M_S$  values for  $\text{Fe}_3\text{O}_4$  nanoparticles prepared with the conventional chemical methods ranged from 30 to 80  $\text{emu/g}$ , with most values being less than 60  $\text{emu/g}$ . The saturation magnetization of  $\text{Fe}_3\text{O}_4$  nanoparticles was measured to be 43.2  $\text{emu/g}$ . Notably, MGONCs possesses the magnetic property (19.8  $\text{emu/g}$ ), which indicated the easy separation advantage by an external magnet instead of the conventional techniques that consume a long time [38].

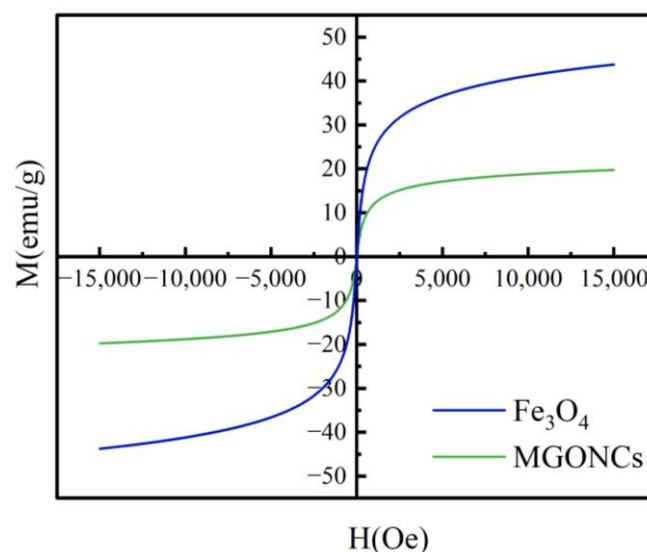


**Figure 7.** Magnetic hysteresis loops of  $\text{Fe}_3\text{O}_4$  and MGONCs.

Indeed, compared to  $\text{Fe}_3\text{O}_4$  particles, the saturation magnetization ( $M_S$ ) value of MGONCs was noticeably lower. This reduction in magnetization could be attributed to the decreased content of magnetic  $\text{Fe}_3\text{O}_4$  in the composite material. However, it was worth noting that the magnetic properties of MGONCs were still sufficient for effective separation using a magnetic separator. The strong magnetism of MGONCs allowed for the easy and rapid separation within 2 s from an aqueous solution.

### 3.1.5. TGA-DSC

TGA-DSC (differential scanning calorimetry) analysis was utilized to measure the weight loss of MGONCs as the temperature increased. The thermal behavior of the MGONCs composite could be divided into three segments, as depicted in the TGA thermogram shown in Figure 8a. The first weight loss, approximately 9.13%, occurred up to 130 °C, which attributed to the evaporation of physically adsorbed water moieties. The second degradation step resulted in a weight loss of about 18.29% up to 340 °C. This weight loss was mainly caused by the breakdown of the biopolymer skeleton structure of GO within the prepared composite. Subsequently, the third degradation step (30.58%) was observed between 340 and 580 °C, which was attributed to the presence of metal oxides within the biopolymer matrix.

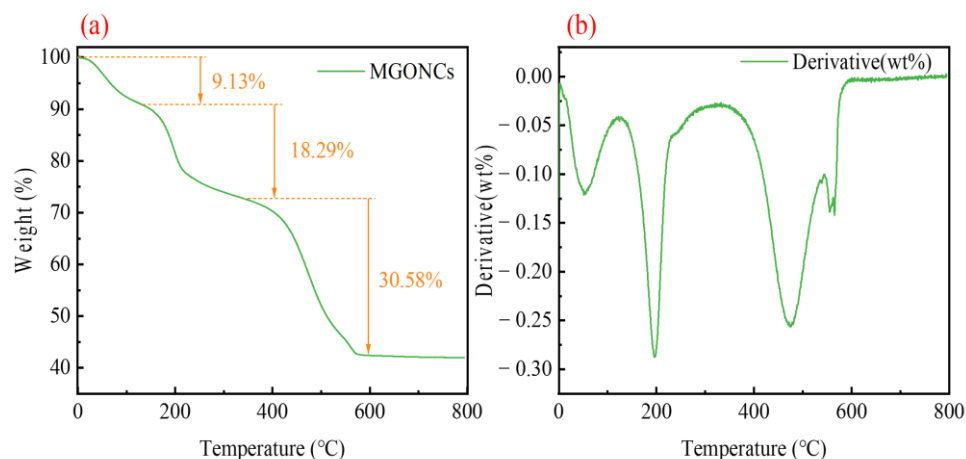


**Figure 8.** Thermal analysis of MGONCs: (a) TGA; (b) DSC.

Afterward, no significant change was observed, indicating the thermal stability of the prepared composite. The DSC thermogram of MGONCs shown in Figure 8b revealed several endothermic peaks. The first endothermic peak, observed at 50–130 °C, corresponded to the release of surface free water molecules. The second endothermic peak at 200 °C was associated with the degradation of polymer backbone chains within the composite. The third endothermic peak occurred at 475 °C, indicating that the MGONCs exhibit good thermal stability [39].

### 3.1.6. BET

The  $\text{N}_2$ -adsorption/desorption isotherm (shown in Figure 9) confirmed that MGONCs composite showed a type II with  $H_4$ -type hysteresis loop, which indicated the mesoporous structure of the composite. Moreover, the specific surface area of MGONCs was 206.4397  $\text{m}^2/\text{g}$ . The results showed that MGONCs obtained a good specific surface area and could be applied for the adsorption of chemical agents.

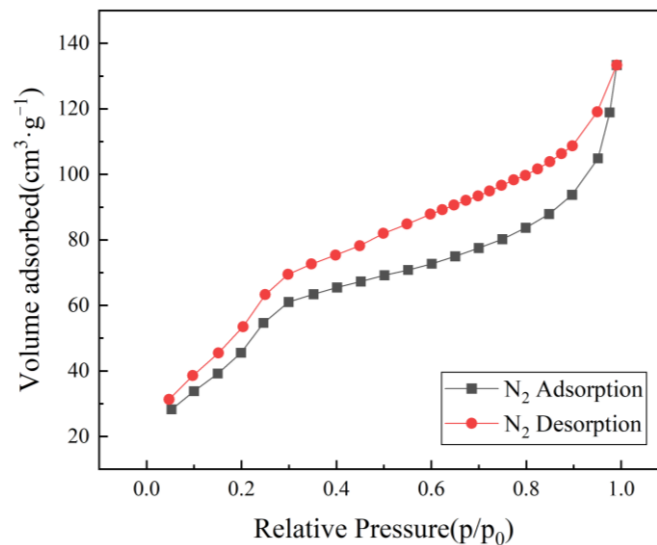


**Figure 9.** N<sub>2</sub>-adsorption/desorption isotherm of MGONCs.

### 3.2. Adsorption of Magnetic Nanomaterials

#### 3.2.1. Effect of Contact Time

The extent of adsorption was mainly dependent on the contact time between the adsorbent and the chemical agents. Therefore, experiments were conducted with an optimized contact time ranging from 0 to 20 min. The adsorption rate curves depicted in Figure 10 indicated that both L and VX consistently maintained a high adsorption rate, with minimal change observed over the course of the adsorption time. This could be attributed to the adsorption behavior being classified as physisorption or physical adsorption. In physisorption, high adsorption rates were achieved through dispersion forces between molecules. Additionally, L was a relatively large molecule with low vapor pressure, and VX was also characterized by its large organic structure and high molar mass. These factors contributed to the ease of physisorption for both L and VX [5]. Physisorption was governed by forces such as long-range London dispersion forces and short-range intermolecular repulsion, which give rise to nonspecific molecular interactions [40]. Furthermore, the MGONCs obtained a high surface area and a mesoporous structure, suggesting that L and VX could easily attach to the surface of the adsorbent during the adsorption process.

In Figure 10, it could be observed that the adsorption rate of GB and GD increased with the increase in adsorption time, but no significant increase was observed beyond 300 s. The initial increase in the adsorption rate with time could be attributed to the greater contact time between the adsorbent and the adsorbate. During the first 300 s, the concentration difference between the bulk solution and the solid–liquid interface led to a rapid adsorption rate. However, after 300 s, the adsorption speed slowed down, likely due to the slower diffusion rate of GB and GD into the interior channels of MGONCs once the surface sites of the adsorbent became saturated with adsorbed targets [41]. To ensure consistent adsorption rates for various chemical agents, an optimized adsorption time of 20 min was established for subsequent studies.

In addition, MGONCs could achieve a complete adsorption of L and VX within 1 min, and near-complete adsorption of GB and GD under 20 min. Meng et al. prepared molecularly imprinted polymers and studied their adsorption of GB, GD, tabun, and VX. It was found that the adsorption tended to be saturated within 16 h. After the 72 h of adsorption, the adsorption rate of VX only reached 25% [42]. Mohammad et al. prepared zirconium hydroxide over woven activated carbon fabric for the adsorption and degradation of chemical warfare agents, which could reach 85% under the condition of 20 min [43]. Compared with the reported research, the MGONCs prepared in our research revealed a better rapid adsorption, which was particularly important for the removal of chemical agents.

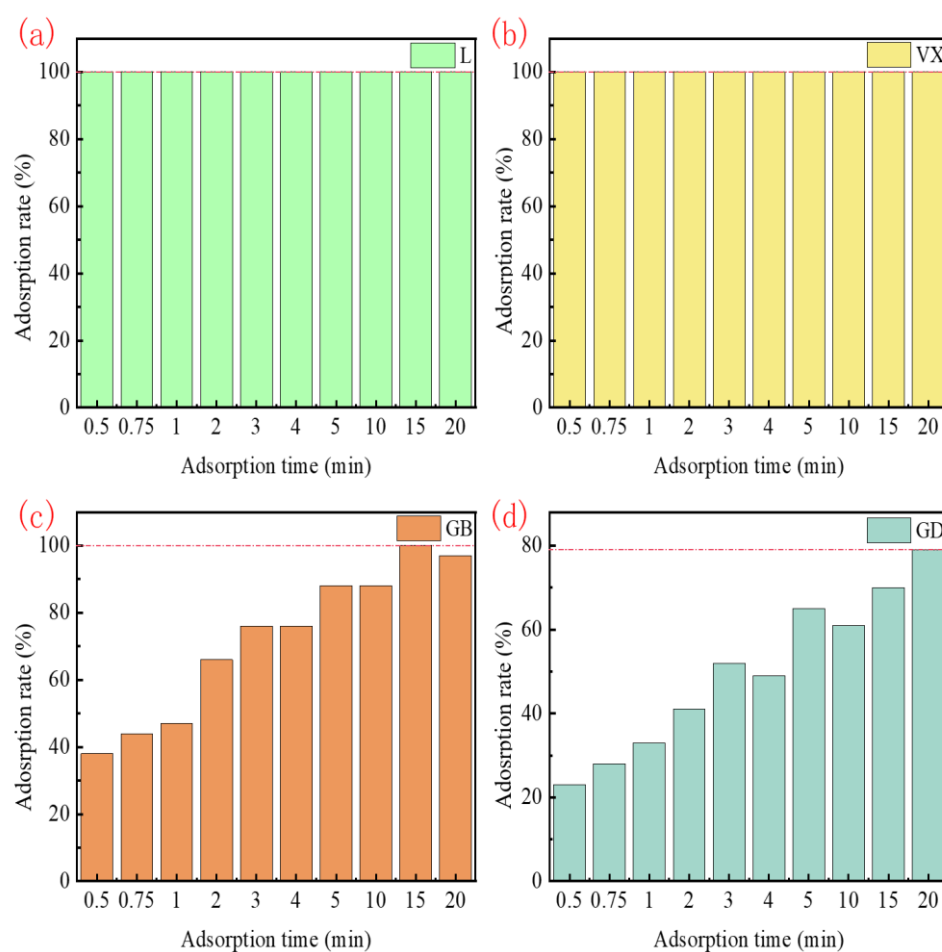


**Figure 10.** Adsorption rate of MGONCs in different adsorption times: (a) for L; (b) for VX; (c) for GB; (d) for GD.

### 3.2.2. Effect of Adsorbent Dosage

Adsorption rates of magnetic composites of different quantities for the chemical agents are shown in Figure 11. The results indicated that L and VX could obtain efficient adsorption when the quantity of magnetic composites was low. In contrast, the adsorption rate of GB and GD increased continuously with the increase in dosage of MGONCs. The various behaviors could be assigned to the increased availability of adsorption sites with the increase in adsorbent dose [44]. The adsorption rate reached nearly 100% under the condition of 20 mg. However, when 10 mg of MGONCs was selected, the adsorption rate of GD is 84%, which meant that the compounds might be unacceptable at the adsorption of 100%. Therefore, 20 mg was applied as the magnetic nanocomposite usage for subsequent studies.

### 3.2.3. Effect of Adsorption Temperature

Temperature was an important parameter during the adsorption process, and the adsorption rate of magnetic composites for selected agents at different temperatures is illustrated in Figure 12. The contact time was set at 20 min, and the adsorbent dosage was 10 mg. The results showed that L, VX, and GB maintained a high adsorption rate across the entire temperature range. On the other hand, the adsorption rate for GD increased with temperature.

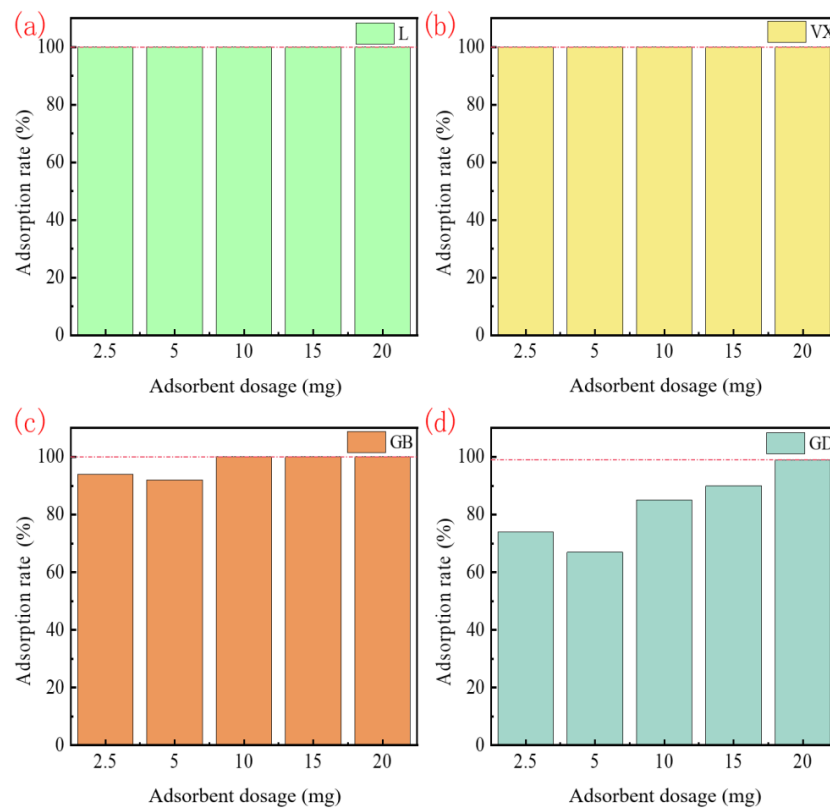


**Figure 11.** Adsorption rate of MGONCs of different adsorbent dosages: (a) for L; (b) for VX; (c) for GB; (d) for GD.

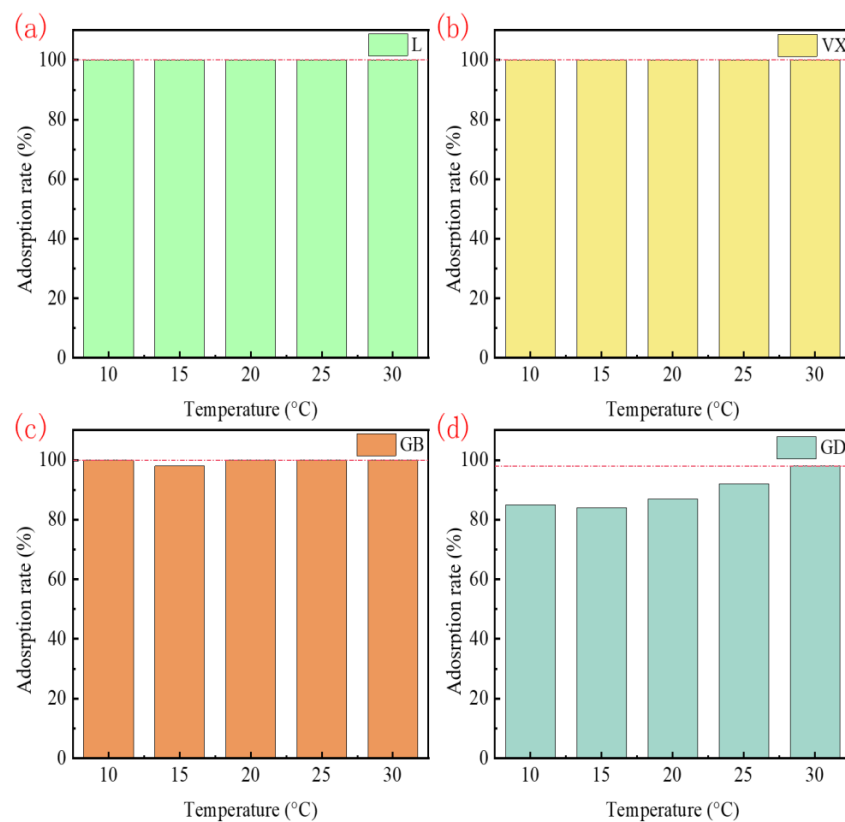


**Figure 12.** Adsorption rate of MGONCs at different adsorption temperatures: (a) for L; (b) for VX; (c) for GB; (d) for GD.

Considering the adsorption curve after adjusting the adsorbent dosage in Section 3.2.2, little influence on the adsorption of L, VX, and GB was observed as the adsorption sites have already reached saturation at 10 mg. However, the temperature had a significant effect on the adsorption rate of GD. The higher temperature led to an increased swelling of the adsorbent, resulting in more active sites being available [45]. The diffusion of GD occurred both externally and internally within the adsorbent. The increasing adsorption capacity with temperature indicated that the adsorption process was identified as an endothermic reaction [44].

### 3.3. Adsorption Kinetics

As mentioned earlier, L and VX exhibit consistently high adsorption rates with little variation observed over different adsorption times. This could be attributed to the adsorption mechanism being physical adsorption, where high adsorption efficiency was achieved through dispersion forces between molecules. Moreover, the magnetic composite nanomaterials possessed a high surface area and mesoporous structure, allowing for a large number of compounds to attach to the adsorption material’s surface.

To assess the kinetics of the adsorption process, two models as the pseudo-first-order model (PFO) and the pseudo-second-order model (PSO) were employed. PFO and PSO were recognized as the classical kinetic models and had been widely applied to investigate the adsorption mechanism by magnetic nanoparticles [46]. These models are described by Equations (3) and (4), respectively. The correlation coefficient ( $R^2$ ) was used to evaluate the goodness of fit for the adsorption kinetic models.

The pseudo-first-order kinetic model assumed that the reaction rate of adsorption was directly proportional to the first power of the adsorbate concentration. The expression of the equation is as follows:

$$q_t = q_e(1 - e^{-K_1t}) \tag{3}$$

where  $q_t$  is the amounts of GB and GD adsorbed (mg/g) at any time  $t$  (min),  $q_e$  is the amounts of phenolic compounds adsorbed (mg/g) at equilibrium, and  $K_1$  ( $\text{min}^{-1}$ ) is the equilibrium rate constant of pseudo-first-order sorption.

On the other hand, the pseudo-second-order model indicated that the adsorption of GB and GD compounds on MGONCs depended on the square of the number of available active sites of the adsorbent [44]. The expression of the equation is as follows:

$$\frac{t}{q_t} = \frac{1}{K_2q_e^2} + \frac{t}{q_e} \tag{4}$$

where  $K_2$  is the rate constant for pseudo-second-order kinetics (g/mg·min).

The calculated kinetics constants and correlation coefficients for the pseudo-first-order (PFO) and pseudo-second-order (PSO) models are presented in Figures 13 and 14 and Table 1. The results indicated that the correlation coefficients ( $R^2$ ) for the PFO model were relatively low, with  $R^2$  values of 0.90089 for GB and 0.86907 for GD. This suggested that the adsorption of GB and GD from MGONCs does not conform well to the PFO model.

**Table 1.** Fitting parameters of adsorption kinetic models.

	PFO			PSO		
	$R^2$	$K_1$ ( $\text{min}^{-1}$ )	$q_e$ (mg/g)	$R^2$	$K_2$ ( $\text{g}\cdot\text{mg}^{-1}\cdot\text{min}^{-1}$ )	$q_e$ (mg/g)
GB	0.90089	0.73516	0.0909	0.99742	8.82163085	0.103125
GD	0.86907	0.52878	0.0680	0.98594	6.79722099	0.081349

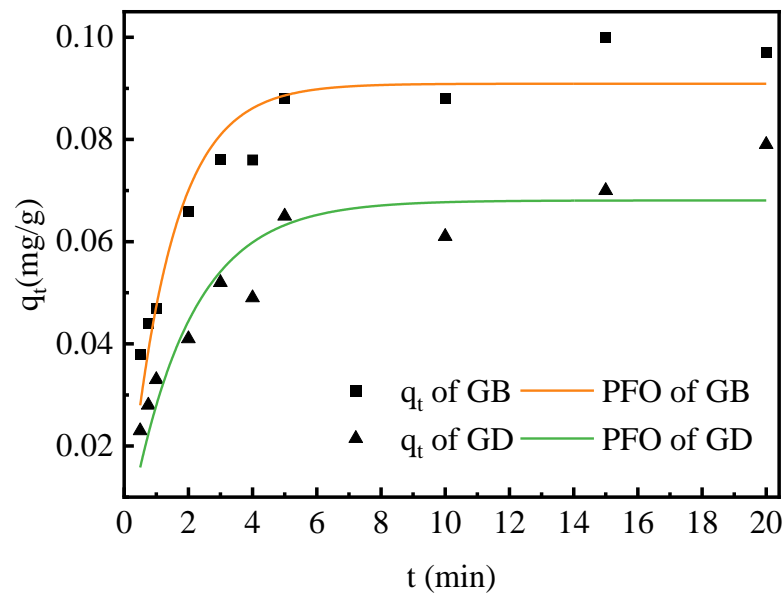


Figure 13. PFO kinetics fitting curve of GB and GD adsorption on MGONCs.

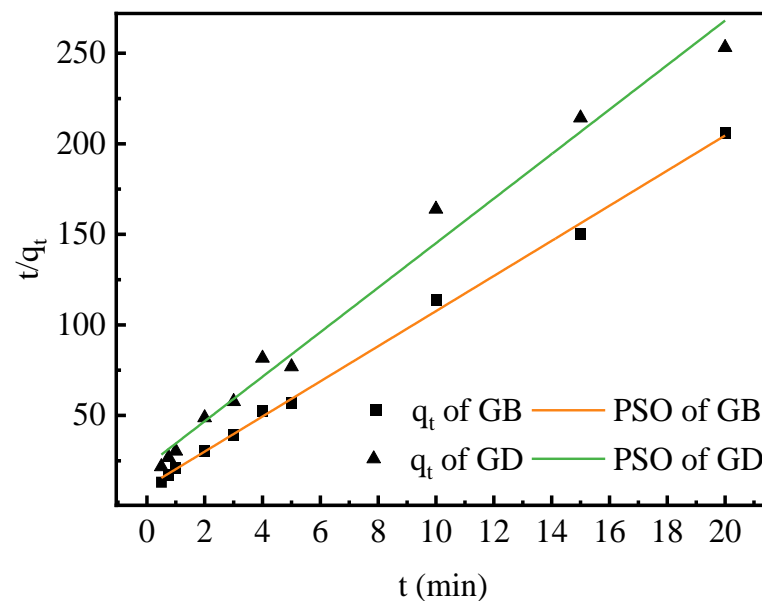


Figure 14. PSO kinetics fitting curve of GB and GD adsorption on MGONCs.

On the other hand, the correlation coefficients obtained for the PSO model were acceptable, with  $R^2$  values of 0.99742 for GB and 0.98594 for GD. These higher  $R^2$  values indicated that the PSO model was more suitable for describing the adsorption of GB and GD on MGONCs. The results suggested that the adsorption mechanism is primarily a chemical process. MGONCs contain a significant number of  $-\text{COOH}$  and  $-\text{OH}$  groups, which enable favorable electrostatic adsorption and hydrogen bonding between the hydroxyl groups and the active functional groups present in MGONCs.

### 3.4. Adsorption Mechanism

The adsorption mechanisms involved in the adsorption process could be attributed to electrostatic attraction, surface complexation, and hydrogen bonding, as illustrated in Figure 15. The  $\text{Fe}_3\text{O}_4$  nanoparticles tend to form complexes through surface complexation and electrostatic interactions with hydroxyl and carboxyl groups present on their surfaces. Consequently, chemical agents could easily form complexes with the MGONCs compos-

ite. Additionally, hydrogen bonding played a role in the adsorption process, wherein the free hydroxyl groups in the MGONCs act as hydrogen bond donors, while the oxygen centers in the chemical agents act as hydrogen bond acceptors. Although the strength of hydrogen bonding was relatively weak compared to other forms of interactions, the presence of numerous potential hydrogen bonding sites contributed to the overall adsorption process [33,37,39].

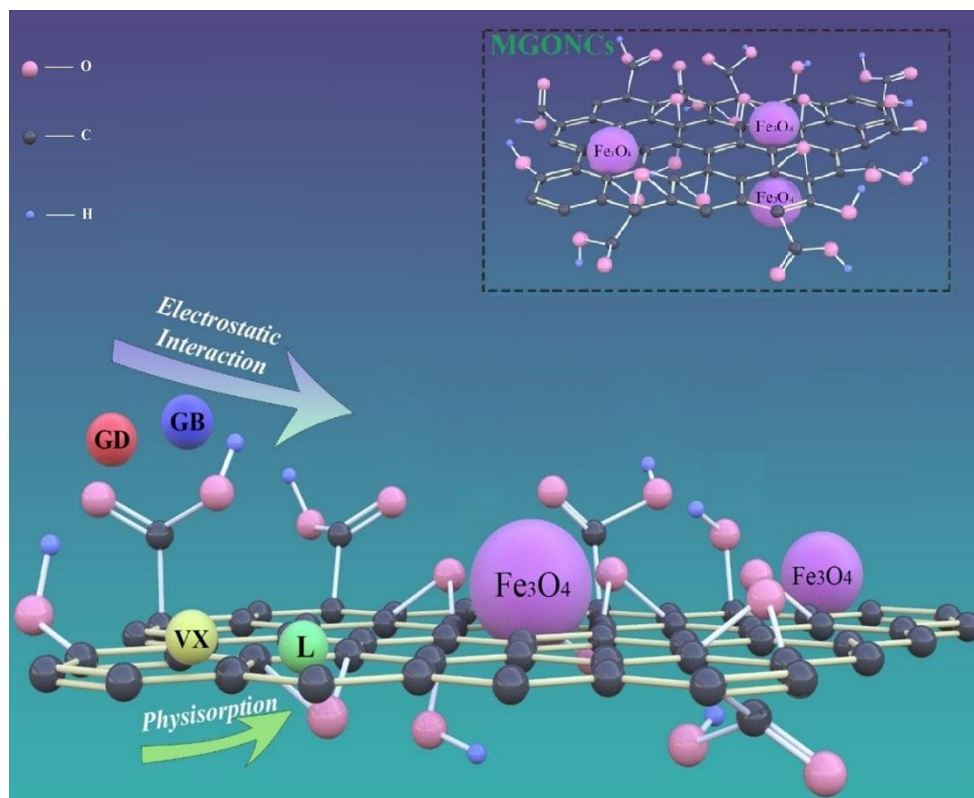


**Figure 15.** Adsorption mechanism of MGONCs adsorb the chemical agents.

#### 4. Conclusions

In our research, we have successfully developed a simple and efficient method for synthesizing the MGONCs adsorbent. This adsorbent can be easily and rapidly separated from dichloromethane solution within a few seconds using an external magnet. The effects of contact time, temperature, and adsorbent dosage have been optimized. The results demonstrate that MGONCs exhibit a high adsorption rate for L, VX, GB, and GD, with the maximum adsorption rate for all four chemical agents being maintained above 99%. The adsorption kinetics behavior of MGONCs for these chemical agents follows the pseudo-second-order (PSO) kinetic model. The major interactions involved in the adsorption mechanisms include electrostatic attraction, surface complexation, and hydrogen bonding. Our research highlights the great potential of MGONCs as an effective adsorbent for the simple and rapid removal of chemical agents from solvents.

**Author Contributions:** Conceptualization, Y.Y.; validation, L.Y.; Material synthesis, R.W. and P.G.; data analysis, G.Q.; writing—original draft preparation, J.W.; writing—review and editing, X.L. All authors have read and agreed to the published version of the manuscript.

**Funding:** This research was funded by [State Key Laboratory of NBC Protection for Civilian], grant number [SKLNBC2021-08].

**Institutional Review Board Statement:** Not applicable.

**Informed Consent Statement:** Not applicable.

**Data Availability Statement:** The data presented in this study are available on request from the corresponding author. The data are not publicly available due to privacy and safety restrictions.

**Conflicts of Interest:** The authors declare no conflict of interest.

## References

1. Yang, Y.C.; Baker, J.A.; Ward, J.R. Decontamination of Chemical Warfare Agents. *Chem. Rev.* **1992**, *92*, 1729–1743. [[CrossRef](#)]
2. Kapp, R.W. Clean Water Act (CWA). *US Encycl. Toxicol.* **2014**, *108*, 979–981.
3. Szinicz, L. History of Chemical and Biological Warfare Agents. *Toxicology* **2005**, *214*, 167–181. [[CrossRef](#)] [[PubMed](#)]
4. Isono, O.; Kituda, A.; Fujii, M.; Yoshinaka, T.; Nakagawa, G.; Suzuki, Y. Long-Term Neurological and Neuropsychological Complications of Sulfur Mustard and Lewisite Mixture Poisoning in Chinese Victims Exposed to Chemical Warfare Agents Abandoned at the End of WWII. *Toxicol. Lett.* **2018**, *293*, 9–15. [[CrossRef](#)] [[PubMed](#)]
5. Lodewyckx, P. *Chapter 10 Adsorption of Chemical Warfare Agents*; Elsevier: Amsterdam, The Netherlands, 2006.
6. Vanninen, P.; Ostin, A.; Beldowski, J.; Pedersen, E.A.; Söderström, M.; Szubska, M.; Grabowski, M.; Siedlewicz, G.; Czub, M.; Popiel, S.; et al. Exposure Status of Sea-Dumped Chemical Warfare Agents in the Baltic Sea. *Mar. Environ. Res.* **2020**, *161*, 105–112. [[CrossRef](#)] [[PubMed](#)]
7. Marrs, T.C.; Maynard, R.L.; Sidell, F.R. *Chemical Warfare Agents, Toxicology and Treatment*; John Wiley & Sons Ltd.: London, UK, 1996.
8. Mohammadnia, E.; Hadavifar, M.; Veisi, H. Kinetics and Thermodynamics of Mercury Adsorption Onto Thiolated Graphene Oxide Nanoparticles. *Polyhedron* **2019**, *173*, 114–139. [[CrossRef](#)]
9. Osovsky, R.; Kaplan, D.; Rotter, H.; Kendler, S.; Goldvaser, M.; Zafrani, Y.; Columbus, I. Hydrothermal Degradation of Adsorbed Sulfur Mustard on Activated Carbon. *Carbon* **2011**, *49*, 3899–3906. [[CrossRef](#)]
10. Kaiser, R.; Kulczyk, A.; Rich, D.; Willey, R.J.; Minicucci, J.; MacIver, B. Effect of Pore Size Distribution of Commercial Activated Carbon Fabrics on the Adsorption of CWA Simulants from the Liquid Phase. *Ind. Eng. Chem. Res.* **2007**, *46*, 6126–6132. [[CrossRef](#)]
11. Sathe, M.; Sharma, P.K.; Singh, V.K.; Tripathi, N.K.; Verma, V.; Sharma, S.P.; Tomar, L.N.S.; Chaturvedi, A.; Yadav, S.S.; Thakare, V.B.; et al. Chemical Protection Studies of Activated Carbon Spheres based Permeable Protective Clothing against Sulfur Mustard, a Chemical Warfare Agent. *Def. Sci. J.* **2019**, *69*, 577–584. [[CrossRef](#)]
12. Sharma, N.; Kakkar, R. Adsorption of Sarin On MgO Nanotubes: Role of Doped and Defect Sites. *J. Comput. Sci.-Neth.* **2015**, *10*, 225–236. [[CrossRef](#)]
13. Kiani, A.; Dastafkan, K. Zinc Oxide Nanocubes as a Destructive Nanoadsorbent for the Neutralization Chemistry of 2-Chloroethyl Phenyl Sulfide: A Sulfur Mustard Simulant. *J. Colloid Interface Sci.* **2016**, *478*, 271–279. [[CrossRef](#)] [[PubMed](#)]
14. Dadvar, S.; Tavanai, H.; Morshed, M.; Ghiaci, M. A Study On the Kinetics of 2-Chloroethyl Ethyl Sulfide Adsorption Onto Nanocomposite Activated Carbon Nanofibers Containing Metal Oxide Nanoparticles. *Sep. Purif. Technol.* **2013**, *114*, 24–30. [[CrossRef](#)]
15. Mahato, T.H.; Prasad, G.K.; Singh, B.; Acharya, J.; Srivastava, A.R.; Vijayaraghavan, R. Nanocrystalline Zinc Oxide for the Decontamination of Sarin. *J. Hazard. Mater.* **2009**, *165*, 928–932. [[CrossRef](#)] [[PubMed](#)]
16. Saxena, A.; Srivastava, A.K.; Singh, B.; Goyal, A. Removal of Sulphur Mustard, Sarin and Simulants on Impregnated Silica Nanoparticles. *J. Hazard. Mater.* **2012**, *211*, 226–232. [[CrossRef](#)] [[PubMed](#)]
17. Panayotov, D.A.; Morris, J.R. Uptake of a Chemical Warfare Agent Simulant (DMMP) on TiO<sub>2</sub>: Reactive Adsorption and Active Site Poisoning. *Langmuir* **2009**, *25*, 3652–3658. [[CrossRef](#)]
18. Son, Y.; Ryu, S.G.; Kim, H.S. Rapid Adsorption and Removal of Sulfur Mustard with Zeolitic Imidazolate Frameworks ZIF-8 and ZIF-67. *Microporous Mesoporous Mater.* **2020**, *293*, 109–119. [[CrossRef](#)]
19. Grissom, T.G.; Plonka, A.M.; Sharp, C.H.; Ebrahim, A.M.; Tian, Y.; Collins-Wildman, D.L.; Kaledin, A.L.; Siegal, H.J.; Troya, D.; Hill, C.L.; et al. Metal–Organic Framework- and Polyoxometalate-Based Sorbents for the Uptake and Destruction of Chemical Warfare Agents. *ACS Appl. Mater. Interfaces* **2020**, *12*, 14641–14661. [[CrossRef](#)]
20. Cho, K.H.; Chitale, S.K.; Kim, S.; Cha, G.; Hong, D.; Ryu, S.G.; Chang, J.; Hwang, Y.K. Adsorptive Removal of Nerve-Agent Simulant with Zirconium-Based Metal–Organic Frameworks Modified by Hydrophobic Monocarboxylic Acids. *Microporous Mesoporous Mater.* **2019**, *285*, 61–69. [[CrossRef](#)]
21. Howarth, A.J.; Majewski, M.B.; Farha, O.K. Metal-organic Frameworks for Capture and Detoxification of Nerve Agents. In *Metal-Organic Frameworks (MOFs) for Environmental Applications*; Elsevier: Amsterdam, The Netherlands, 2019; pp. 179–202.
22. Yu, H.; Son, Y.R.; Yoo, H.; Cha, H.G.; Lee, H.; Kim, H.S. Chitosan-Derived Porous Activated Carbon for the Removal of the Chemical Warfare Agent Simulant Dimethyl Methylphosphonate. *Nanomaterials* **2019**, *9*, 1703. [[CrossRef](#)]
23. Florent, M.; Giannakoudakis, D.A.; Wallace, R.; Bandosz, T.J. Mixed CuFe and ZnFe (Hydr)oxides as Reactive Adsorbents of Chemical Warfare Agent Surrogates. *J. Hazard. Mater.* **2017**, *329*, 141–149. [[CrossRef](#)]
24. You, X.; He, M.; Cao, X.; Wang, P.; Wang, J.; Li, L. Molecular Dynamics Simulations of Removal of Nonylphenol Pollutants by Graphene Oxide: Experimental Study and Modelling. *Appl. Surf. Sci.* **2019**, *475*, 621–626. [[CrossRef](#)]
25. Dikin, D.A.; Stankovich, S.; Zimney, E.J.; Piner, R.D.; Dommert, G.H.B.; Evmenenko, G.; Nguyen, S.T.; Ruoff, R.S. Preparation and characterization of graphene oxide paper. *Nature* **2007**, *448*, 457–460. [[CrossRef](#)] [[PubMed](#)]

26. Dreyer, D.R.; Park, S.; Bielawski, C.W.; Ruoff, R.S. The Chemistry of Graphene Oxide. *Chem. Soc. Rev.* **2010**, *39*, 228–240. [[CrossRef](#)] [[PubMed](#)]
27. Li, Y.; Ju, W.; Yang, L.; Zhang, L.; Sun, Y. Adsorption Behaviors and Mechanism of Graphene Oxide for Silver Complex Anion Removal. *Appl. Surf. Sci.* **2020**, *529*, 112–147. [[CrossRef](#)]
28. Zhao, G.; Li, J.; Ren, X.; Chen, C.; Wang, X. Few-Layered Graphene Oxide Nanosheets as Superior Sorbents for Heavy Metal Ion Pollution Management. *Environ. Sci. Technol.* **2011**, *45*, 10454–10462. [[CrossRef](#)]
29. Bolibok, P.; Koter, S.; Kaczmarek, K.A.; Kowalczyk, P.; Lukomska, B.; Lukomska, O.; Boncel, S.; Wiśniewski, M.; Kaneko, K.; Terzyk, A.P. Liquid Phase Adsorption Induced Nanosizing of Graphene Oxide. *Carbon* **2021**, *183*, 948–957. [[CrossRef](#)]
30. Singh, S.; Anil, A.G.; Khasnabis, S.; Kumar, V.; Nath, B.; Adiga, V.; Naik, T.S.S.K.; Subramanian, S.; Kumar, V.; Singh, J.; et al. Sustainable Removal of Cr(VI) Using Graphene Oxide-Zinc Oxide Nanohybrid: Adsorption Kinetics, Isotherms and Thermodynamics. *Environ. Res.* **2022**, *203*, 111891. [[CrossRef](#)]
31. Henych, J.; Stengl, V.; Mattsson, A.; Tolasz, J.; Osterlund, L. Chemical Warfare Agent Simulant DMMP Reactive Adsorption on TiO<sub>2</sub>/graphene Oxide Composites Prepared via Titanium Peroxo-Complex Or Urea Precipitation. *J. Hazard. Mater.* **2018**, *359*, 482–490. [[CrossRef](#)]
32. Stastny, M.; Tolasz, J.; Stengl, V.; Henych, J.; Zizka, D. Graphene oxide/MnO<sub>2</sub> Nanocomposite as Destructive Adsorbent of Nerve-Agent Simulants in Aqueous Media. *Appl. Surf. Sci.* **2017**, *412*, 19–28. [[CrossRef](#)]
33. Neolaka, Y.A.B.; Lawa, Y.; Naat, J.N.; Riwu, A.A.P.; Iqbal, M.; Darmokoesoemo, H.; Kusuma, H.S. The Adsorption of Cr(VI) From Water Samples Using Graphene Oxide-Magnetic (GO-Fe<sub>3</sub>O<sub>4</sub>) Synthesized From Natural Cellulose-Based Graphite (Kusambi Wood Or Schleichera Oleosa): Study of Kinetics, Isotherms and Thermodynamics. *J. Mater. Res. Technol.* **2020**, *9*, 6544–6556. [[CrossRef](#)]
34. Petcharoen, K.; Sirivat, A. Synthesis and Characterization of Magnetite Nanoparticles via the Chemical Co-Precipitation Method. *Mater. Sci. Eng. B* **2012**, *177*, 421–427. [[CrossRef](#)]
35. Ricardo, A.I.C.; Abujaber, F.; Bernardo, F.J.G.; Martin-Doimeadios, R.C.R.; Rios, A. Magnetic Solid Phase Extraction as a Valuable Tool for Elemental Speciation Analysis. *Trends Environ. Anal.* **2020**, *27*, e00097. [[CrossRef](#)]
36. Huang, G.; Lu, C.; Yang, H. *Chapter 3—Magnetic Nanomaterials for Magnetic Bioanalysis*; Elsevier: Amsterdam, The Netherlands, 2019.
37. Mallesh, S.; Jang, W.; Kim, K.H. Facile Synthesis of Cube-Like Fe<sub>3</sub>O<sub>4</sub>-graphene Oxide Nanocomposites with Excellent Microwave Absorption Performance. *Phys. Lett. A* **2021**, *389*, 127069. [[CrossRef](#)]
38. El-Monaem, E.M.A.; Eltaweil, A.S.; El-Subruiti, G.M.; Mohy-Eldin, M.S.; Omer, A.M. Adsorption of nitrophenol onto a novel Fe<sub>3</sub>O<sub>4</sub>-κ-carrageenan/MIL-125(Ti) composite: Process optimization, isotherms, kinetics, and mechanism. *Environ. Sci. Pollut. Res.* **2023**, *30*, 49301–49313. [[CrossRef](#)]
39. Sirajudheen, P.; Nikitha, M.R.; Karthikeyan, P.; Meenakshi, S. Perceptive Removal of Toxic Azo Dyes from Water Using Magnetic Fe<sub>3</sub>O<sub>4</sub> Reinforced Graphene Oxide–Carboxymethyl Cellulose Recyclable Composite: Adsorption Investigation of Parametric Studies and their Mechanisms. *Surf. Interfaces* **2020**, *21*, 100648. [[CrossRef](#)]
40. Thommes, M.; Cychosz, K.A.; Neimark, A.V. *Chapter 4—Advanced Physical Adsorption Characterization of Nanoporous Carbons*; Elsevier: Amsterdam, The Netherlands, 2012.
41. Khanday, W.A.; Majid, S.A.; Shekar, S.C.; Tomar, R. Dynamic Adsorption of DMMP over Synthetic zeolite-Alpha. *Arab. J. Chem.* **2014**, *7*, 115–123. [[CrossRef](#)]
42. Meng, Z.H.; Zhao, Y.X.; Feng, J.L.; Liu, Y.T.; Yun, L.H.; Ruan, J.X. The research of adsorption of organophosphorus toxicants on molecule imprinting polymers. *Chin. J. Anal. Chem.* **2000**, *28*, 432–435.
43. Imran, M.; Singh, V.V.; Garg, P.; Mazumder, A.; Pandey, L.K.; Sharma, P.K.; Acharya, J.; Ganesan, K. In-situ detoxification of schedule-I chemical warfare agents utilizing Zr(OH)<sub>4</sub>@W-ACF functional material for the development of next generation NBC protective gears. *Sci. Rep.* **2021**, *11*, 24421. [[CrossRef](#)]
44. Elayadi, F.; Boumya, W.; Achak, M.; Chhiti, Y.; Alaoui, F.E.M.; Barka, N.; Adlouni, C.E. Experimental and Modeling Studies of the Removal of Phenolic Compounds from Olive Mill Wastewater by Adsorption On Sugarcane Bagasse. *Environ. Chall.* **2021**, *4*, 100184. [[CrossRef](#)]
45. Han, Q.; Yang, L.; Liang, Q.L.; Ding, M.Y. Three-dimensional hierarchical porous graphene aerogel for efficient adsorption and preconcentration of chemical warfare agents. *Carbon* **2017**, *122*, 556–563. [[CrossRef](#)]
46. Lin, S.; Lu, D.; Liu, Z. Removal of arsenic contaminants with magnetic c-Fe<sub>2</sub>O<sub>3</sub> nanoparticles. *Chem. Eng. J.* **2012**, *211*, 46–52. [[CrossRef](#)]

**Disclaimer/Publisher’s Note:** The statements, opinions and data contained in all publications are solely those of the individual author(s) and contributor(s) and not of MDPI and/or the editor(s). MDPI and/or the editor(s) disclaim responsibility for any injury to people or property resulting from any ideas, methods, instructions or products referred to in the content.